Atomic-scale identification of the active sites of nanocatalysts

Yao Yang
University of California Los Angeles https://orcid.org/0000-0002-2896-9046
Jihan Zhou
Peking Univeristy
Zipeng Zhao
University of California Los Angeles
Geng Sun
University of California Los Angeles
Saman Moniri
University of Michigan&#x2013 https://orcid.org/0000-0003-0723-5091
Colin Ophus
National Center for Electron Microscopy Facility, Molecular Foundry, Lawrence Berkeley National Laboratory
Yongsoo Yang
Korea Advanced Institute of Science and Technology (KAIST) https://orcid.org/0000-0001-8654-302X
Ziyang Wei
University of California Los Angeles
Yakun Yuan
University of California Los Angeles
Cheng Zhu
University of Colorado at Boulder https://orcid.org/0000-0002-4772-970X
Yang Liu
University of California Los Angeles
Qiang Sun
Northeastern University
Qingying Jia
Northeastern University https://orcid.org/0000-0002-4005-8894
Hendrik Heinz
University of Colorado Boulder https://orcid.org/0000-0002-6776-7404
Jim Ciston
Lawrence Berkeley National Laboratory https://orcid.org/0000-0002-8774-5747
Peter Ercius
Lawrence Berkeley National Laboratory https://orcid.org/0000-0002-6762-9976

Philippe Sautet
University of California Los Angeles https://orcid.org/0000-0002-8444-3348
Yu Huang
University of California Los Angeles https://orcid.org/0000-0003-1793-0741
Jianwei (John) Miao (miao@physics.ucla.edu)
University of California Los Angeles https://orcid.org/0000-0003-4033-3945

Letter

Keywords:

Posted Date: August 4th, 2022

DOI: https://doi.org/10.21203/rs.3.rs-1471299/v2

Atomic-scale identification of the active sites of nanocatalysts

Yao Yang[1,8], Jihan Zhou[1,8], Zipeng Zhao[2,8], Geng Sun[3,8], Saman Moniri[1], Colin Ophus[4], Yongsoo Yang[1], Ziyang Wei[5], Yakun Yuan[1], Cheng Zhu[6], Yang Liu[2], Qiang Sun[7], Qingying Jia[7], Hendrik Heinz[6], Jim Ciston[4], Peter Ercius[4], Philippe Sautet[3,5], Yu Huang[2], Jianwei Miao[1*]

[1]*Department of Physics & Astronomy and California NanoSystems Institute, University of California, Los Angeles, CA 90095, USA.* [2]*Department of Materials Science and Engineering, University of California, Los Angeles, CA 90095, USA.* [3]*Department of Chemical and Biomolecular Engineering, University of California, Los Angeles, Los Angeles, CA 90095, USA.* [4]*National Center for Electron Microscopy, Molecular Foundry, Lawrence Berkeley National Laboratory, Berkeley, CA 94720, USA.* [5]*Department of Chemistry and Biochemistry, University of California, Los Angeles, Los Angeles, CA 90095, USA.* [6]*Department of Chemical and Biological Engineering, University of Colorado at Boulder, Boulder, CO, USA.* [7]*Department of Chemistry and Chemical Biology, Northeastern University, Boston, MA, USA*

[8]*These authors contributed equally to this work.* [*]*e-mail: miao@physics.ucla.edu*

Heterogeneous catalysts play a key role in the chemical and energy industries[1]. To date, most industrial-scale heterogeneous catalytic reactions have relied on nanocatalysts[2,3]. However, despite significant progress from theoretical, experimental and computational studies[4-18], identifying the active sites of alloy nanocatalysts remains a major challenge. This limitation is mainly due to an incomplete understanding of the three-dimensional (3D) atomic and chemical arrangement of different constituents and structural reconstructions driven by catalytic reactions[19-22]. Here, we use atomic electron tomography[23] to determine the

3D local atomic structure, surface morphology and chemical composition of 11 Pt alloy nanocatalysts for the electrochemical oxygen reduction reaction (ORR). We reveal the facet, surface concaveness, structural and chemical order/disorder, coordination number, and bond length with unprecedented 3D atomic detail. The experimental 3D atomic coordinates are used by first-principles trained machine learning to identify the active sites of the nanocatalysts, which are corroborated by electrochemical measurements. A striking feature is the difference of the ORR activity of the surface Pt sites on the nanocatalysts by several orders of magnitude. Furthermore, by analyzing the structure-activity relationship, we formulate an equation named the local environment descriptor to balance the strain and ligand effects and gain quantitative insights into the ORR active sites of the Pt alloy nanocatalysts. The ability to determine the 3D atomic structure and chemical composition of realistic nanoparticles coupled with machine learning could transform our fundamental understanding of the catalytic active sites and provide a guidance for the rational design of optimal nanocatalysts.

PtNi and Mo-doped PtNi (Mo-PtNi) nanocatalysts with varying Ni concentration were synthesized on carbon black / nanotubes using an efficient one-pot approach[24,25] (Methods). The nanocatalysts on carbon black were activated through a cyclic voltammetry test, and the ORR specific activities of PtNi and Mo-PtNi were measured to be 4.8 and 9.3 mA/cm^2 at 0.9 V_{RHE}, respectively (Supplementary Fig. 1). The increase of the ORR activity with Mo dopants is consistent with previous reports[24-26]. Atomic electron tomography (AET) experiments were performed on 11 nanocatalysts embedded in carbon nanotubes with an annular dark-field scanning transmission electron microscope (Supplementary Figs. 2-6 and Table 1). By using a low-exposure data

acquisition scheme[27] and minimizing the electron dose, the structure of the nanocatalysts were consistent throughout the experiment (Supplementary Fig. 7). After pre-processing, 3D reconstruction, atom tracing and refinement[23,28] (Methods and Supplementary Fig. 8), the 3D atomic coordinates and chemical composition of the nanocatalysts were determined (Fig. 1), where the voxel size was calibrated by an extended x-ray absorption fine structure measurement (Methods). The total number of the Pt and Ni atoms in each of the 11 nanocatalysts ranges from 4,281 to 14,172 (Supplementary Table 1). Due to a very small fraction (~0.4%) of Mo dopants[25], AET is presently not sensitive enough to distinguish them from the Ni or Pt atoms, but this limitation will not impact the conclusions of this study.

Figure 1, Supplementary Fig. 9 and Video 1 show the 3D surface morphology, atomic structure and chemical composition of the 11 PtNi and Mo-PtNi nanocatalysts. Elemental segregation was observed on the surface and in the interior of the nanoparticles. The surface layer mainly consists of Pt atoms, forming (100), (110), (111) and a small fraction of high-index facets. From the experimental 3D coordinates, we quantitatively characterized the surface concaveness, structural and chemical order/disorder, coordination number (CN), and surface bond length (Methods). Although the majority of the nanoparticles exhibit an octahedral morphology, we observed surface concaveness, structural and chemical disorder to varying degrees in all these nanocatalysts (Fig. 2a-c). We revealed that the Mo dopants increase the surface concaveness and the structural disorder and preserved more subsurface Ni atoms (Fig. 2a, b and d). The CN of the surface Pt sites ranges from 4 to 11 with the peak at CN = 9 (Fig. 2e). The average surface Pt-Pt bond length was measured to be 2.77±0.16 Å and 2.75±0.19 Å for PtNi and Mo-PtNi, respectively (Fig. 2f), which are correlated with the subsurface Ni composition. The

increase of the subsurface Ni composition reduces the average surface Pt-Pt bond length (Fig. 2g).

The experimentally determined 3D atomic coordinates were used by first-principles trained machine learning (ML) to identify the ORR active sites of the nanocatalysts (Methods). The ORR takes place primarily through a four-step electroreduction mechanism $O_2 + 4\ (H^+ + e^-) \rightarrow 2H_2O$, in which the surface hydroxyl group (OH) is an intermediate[14]. Density functional theory (DFT) calculations have revealed that the ORR activity follows the Sabatier principle[11,14,29], that is, the optimal catalysts have the adsorption energy of the intermediates neither too strong nor too weak. When the OH binding energy (BE_{OH}) is about 0.13 eV weaker than that of bulk Pt(111), the optimal ORR activity is reached[11,14]. As it is computationally impractical to perform DFT calculations for all the 11 nanocatalysts each with several thousands of atoms, we used a DFT-trained ML method to determine the OH binding energy for the experimentally measured surface Pt sites (Methods). We first constructed 207 3D PtNi atomic models each surrounding a surface Pt site with a different local environment (Supplementary Fig. 10). After calculating the BE_{OH} for the 207 Pt sites by DFT, we randomly chose 134 sites to train the ML method and then used it to identify the BE_{OH} of the 73 test Pt sites. A quantitative comparison between the DFT calculated and ML identified BE_{OH} is shown in Supplementary Fig. 11, indicating that ML accurately predicted the BE_{OH} with a root mean square error (RMSE) of 0.05 and 0.07 eV per site for the 134 training and 73 test Pt sites, respectively.

After training and validating the ML method, we applied it to evaluate the ORR activity for the experimentally measured surface Pt sites of the PtNi and Mo-PtNi nanocatalysts. By referring BE_{OH} to the OH binding energy of Pt(111)[14], we identified

97 the ORR activity for all the surface Pt sites (Methods). The average catalytic activities of
98 the 11 nanocatalysts agree well with the electrochemical measurements (Fig. 3a),
99 showing the robustness of using DFT-trained ML to identify the ORR activity for the
100 experimental 3D atomic coordinates. Figure 3b, c, Supplementary Video 2, and
101 Supplementary Fig. 12 show the ORR activity maps of the surface Pt sites of the 11 PtNi
102 and Mo-PtNi nanocatalysts. We observed that the ORR activity of the surface Pt sites
103 varies by several orders of magnitude. While the majority of the surface Pt sites have a
104 low catalytic activity, there are a very small fraction of highly active sites (yellow atoms
105 in Fig. 3b and c). Figure 3d-i shows six representative highly active sites on the PtNi and
106 Mo-PtNi nanocatalysts, each of which exhibits a distinct 3D local environment such as
107 different CN, neighbouring Ni atoms and surface morphology. This observation indicates
108 that quantitative characterization of the 3D local atomic environment is critical to the
109 understanding of the active sites of nanocatalysts.

110 To gain quantitative insights into the ORR active sites of the nanocatalysts, we
111 performed a comprehensive analysis of the structure-activity relationship at the individual
112 atom level. We fit a large number of experimentally measured structural and chemical
113 properties such as the surface concaveness, CN, Pt-Pt bond length, structure/chemical
114 order parameters, strain/ligand effects, and others to the ΔBE_{OH} of the 26,246 surface Pt
115 sites of the PtNi and Mo-PtNi nanocatalysts (Methods and Supplementary Tables 2). By
116 minimizing the RMSE between the calculated and ML-determined ΔBE_{OH}, we derived
117 the local environment descriptor (LED) (Methods), which is dimensionless and defined
118 as,

119 $$\mathrm{LED} = \mathrm{NN}^{\mathrm{Pt}} \cdot \mathrm{e}^{-a_1 \cdot \varepsilon} + a_2 \cdot \overline{\mathrm{CN}}^{\mathrm{Ni}}, \quad (1)$$

Where NN^{Pt} is the number of the nearest-neighbour Pt atoms of a surface Pt site, $\varepsilon = \frac{\bar{d}_{Pt}-d_0}{d_0}$ is the local strain with $\bar{d}_{Pt}$ the average Pt-Pt bond length around the surface Pt site and d_0 the Pt-Pt bond length (2.75 Å) for Pt nanocrystals, $\overline{CN}^{Ni} = \sum_i \frac{CN_i^{Ni}}{CN_{max}}$ is the generalized CN of the considered Pt with Ni atoms[11,30], CN_i^{Ni} is the CN of the i^{th} Ni atom, $CN_{max} = 12$ is the CN in bulk Pt, a_1 and a_2 are two fitting constants related to the strain and ligand effects, respectively. Our quantitative analysis showed that NN^{Pt}, $\bar{d}_{Pt}$ and $\overline{CN}^{Ni}$ are more relevant to the ORR activity of the nanocatalysts than other properties such as surface concaveness, structural and chemical order/disorder (Methods). By fitting the LED to the BE_{OH} of all the surface Pt sites relative to the OH binding energy of Pt(111), we obtained the distribution of the ORR activity as a function of the LED, showing a volcano plot with the peak at LED = 9.7 (dashed red line in Fig. 3j). The RMSE of the fitting is 0.104 eV with a_1 = 1.985 and a_2 = 1.075. The small RMSE value indicates the robustness of the structure-activity fitting analysis. Figure 3k, l, Supplementary Fig. 13, and Video 2 show the activity maps of the 11 PtNi and Mo-PtNi nanocatalysts based on the LED, which agree well with ML-identified activity maps (Fig. 3b, c and Supplementary Fig. 12). As specific examples, the six highly active sites shown in Fig. 3d-i has the LED between 9.7 and 9.79.

To better understand the LED, we considered a Pt(111) surface without strain. From Eq. (1), we calculated LED = 9, which is located on the left-side of the peak of the volcano plot (Fig. 3j). If a nearest-neighbour surface Pt atom is substituted by a Ni atom, the first term of Eq. (1) decreases by 1, but the second term increases by a number smaller than 1, making LED smaller than 9 and decreasing the activity. If the substitutional Ni atom is in the subsurface, the CN of the Ni is 12 and the second term increases by a

number larger than 1 as $a_2 > 1$, making LED larger than 9. Furthermore, compressive strain, induced by the decrease of the average Pt-Pt bond length, also increases LED. Consequently, with LED < 9.7, both subsurface Ni atoms and compressive strain increase the ORR activity. When LED reaches the peak of the volcano plot (LED = 9.7 in Fig. 3j), further increasing the subsurface Ni atoms and the compressive strain reduces the ORR activity. Thus, the LED quantitatively balances the strain and ligand effects to optimize the ORR activity of PtNi and Mo-PtNi nanocatalysts.

Our experimental results revealed that statistically Mo-PtNi has a shorter surface Pt-Pt bond length and a broader distribution than PtNi (Fig. 2f), indicating that Mo-PtNi presents a larger compressive strain than PtNi. Additionally, Mo-PtNi preserves more subsurface Ni atoms than PtNi (Fig. 2d). According to Eq. (1), both factors increase the LED of Mo-PtNi over PtNi. As the measured and the ML-identified ORR activity of Mo-PtNi are higher than those of PtNi (Fig. 3a), our observations indicate that the average catalytic activity of the Mo-PtNi and PtNi nanocatalysts is situated on the left-side of the peak of the volcano (Fig. 3j), which can explain previous experimental results that a larger concentration of Co or Ni in Pt-alloy nanocatalysts increases the ORR activity[31,32]. Although we focused on PtNi and Mo-PtNi nanoparticles in this study, our approach to constructing the LED is applicable to other nanocatalysts.

In conclusion, we determined the 3D local atomic structure and chemical composition of PtNi and Mo-PtNi nanocatalysts each comprising a few thousands of atoms. We measured the facets, surface concaveness, structural and chemical order/disorder, CN, and bond lengths with high precision. From the experimentally measured 3D atomic coordinates, we used a DFT-trained ML method to identify the active sites of the 11 nanocatalysts, which were validated by electrochemical

measurements. By performing a comprehensive analysis of the structure-activity relationship, we derived the LED to quantitatively characterize the ORR activity of the nanocatalysts based on the surface, subsurface atomic structure and chemical composition. We found that the nearest-neighbour surface Pt atoms, the average Pt-Pt bond length and the generalized CN for Ni neighbours are the most relevant parameters for the ORR activity. The optimal reactivity is achieved with the right balance between the ligand and strain effects, with subsurface Ni ligands behaving differently from surface ones. We expect that this work paves the way to measure the 3D local atomic positions, chemical species and surface composition of a wide range of nanocatalysts for various (electro)chemical reactions and to correlate the 3D atomic structure with the catalytic activity at the single-atom level.

References

1. Friend, C. M. & Xu, B. Heterogeneous Catalysis: A Central Science for a Sustainable Future. *Acc. Chem. Res.* **50**, 517-521 (2017).
2. Astruc, D. Introduction: Nanoparticles in Catalysis. *Chem. Rev*. **120**, 461–463 (2020).
3. Mitchell, S., Qin, R., Zheng, N. & Pérez-Ramírez, J. Nanoscale engineering of catalytic materials for sustainable technologies. *Nat. Nanotechnol.* **16**, 129-139 (2021).
4. Stamenkovic, V. R. *et al.* Improved oxygen reduction activity on $Pt_3Ni(111)$ via increased surface site availability. *Science* **315**, 493-497 (2007).
5. Nørskov, J. K. *et al.* The nature of the active site in heterogeneous metal catalysis. *Chem. Soc. Rev.* **37**, 2163-2171 (2008).

6. de Smit, E. *et al.* Nanoscale chemical imaging of a working catalyst by scanning transmission X-ray microscopy. *Nature* **456**, 222-225 (2008).
7. Greeley, J. *et al.* Alloys of platinum and early transition metals as oxygen reduction electrocatalysts. *Nat. Chem.* **1**, 552-556 (2009).
8. Strasser, P. *et al.* Lattice-strain control of the activity in dealloyed core–shell fuel cell catalysts. *Nat. Chem.* **2**, 454-460 (2010).
9. Lamberti, C., Zecchina, A., Groppo, E. & Bordiga, S. Probing the surfaces of heterogeneous catalysts by in situ IR spectroscopy. *Chem. Soc. Rev.* **39**, 4951-5001 (2010).
10. Chen, C. *et al.* Highly Crystalline Multimetallic Nanoframes with Three-Dimensional Electrocatalytic Surfaces. *Science* **343**, 1339-1343 (2014).
11. Calle-Vallejo, F. *et al.* Finding optimal surface sites on heterogeneous catalysts by counting nearest neighbors. *Science* **350**, 185-189 (2015).
12. Zhang, L. *et al.* Platinum-based nanocages with subnanometer-thick walls and well-defined, controllable facets. *Science* **349**, 412-416 (2015).
13. Escudero-Escribano, M. *et al.* Tuning the activity of Pt alloy electrocatalysts by means of the lanthanide contraction. *Science* **352**, 73-76 (2016).
14. Kulkarni, A., Siahrostami, S., Patel, A. & Nørskov, J. K. Understanding Catalytic Activity Trends in the Oxygen Reduction Reaction. *Chem. Rev.* **118**, 2302-2312 (2018).
15. Núñez, M. Lansford, J. L. & Vlachos, D. G. Optimization of the facet structure of transition-metal catalysts applied to the oxygen reduction reaction. *Nat. Chem.* **11**, 449-456 (2019).

16. Wang, L. *et al.* Tunable intrinsic strain in two-dimensional transition metal electrocatalysts. *Science* **363**, 870-874 (2019).
17. Kim, S. *et al.* Correlating 3D Surface Atomic Structure and Catalytic Activities of Pt Nanocrystals. *Nano Lett.* **21**, 1175-1183 (2021).
18. Lee, J., Jeong, C., Lee, T., Ryu, S. & Yang, Y. Direct Observation of Three-Dimensional Atomic Structure of Twinned Metallic Nanoparticles and Their Catalytic Properties. *Nano Lett.* **22**, 665-672 (2022).
19. Tao, F. *et al.* Reaction-Driven Restructuring of Rh-Pd and Pt-Pd Core-Shell Nanoparticles. *Science* **322**, 932-934 (2008).
20. Cui, C., Gan, L., Heggen, M., Rudi, S. & Strasser, P. Compositional segregation in shaped Pt alloy nanoparticles and their structural behaviour during electrocatalysis. *Nat. Mater.* **12**, 765-771 (2013).
21. Zugic, B. *et al.* Dynamic restructuring drives catalytic activity on nanoporous gold–silver alloy catalysts. *Nat. Mater.* **16**, 558-564 (2017).
22. Jacobse, L., Huang, Y.-F., Koper, M. T. M. & Rost, M. J. Correlation of surface site formation to nanoisland growth in the electrochemical roughening of Pt(111). *Nat. Mater.* **17**, 277-282 (2018).
23. Miao, J., Ercius, P. & Billinge, S. J. Atomic electron tomography: 3D structures without crystals. *Science* **353**, aaf2157 (2016).
24. Huang, X. *et al.* High-performance transition metal–doped Pt_3Ni octahedra for oxygen reduction reaction. *Science* **348**, 1230-1234 (2015).
25. Jia, Q. *et al.* Roles of Mo Surface Dopants in Enhancing the ORR Performance of Octahedral PtNi Nanoparticles. *Nano Lett.* **18**, 798-804 (2018).

26. Dionigi, F. *et al.* Controlling Near-Surface Ni Composition in Octahedral PtNi(Mo) Nanoparticles by Mo Doping for a Highly Active Oxygen Reduction Reaction Catalyst. *Nano Lett.* **19**, 6876-6885 (2019).

27. Scott, M. C. *et al*. Electron tomography at 2.4-ångström resolution. *Nature* **483**, 444-447 (2012).

28. Yang, Y. *et al.* Determining the three-dimensional atomic structure of an amorphous solid. *Nature* **592**, 60-64 (2021).

29. Nørskov, J. K. *et al.* Origin of the Overpotential for Oxygen Reduction at a Fuel-Cell Cathode. *J. Phys. Chem. B* **108**, 17886-17892 (2004).

30. Nanba, Y. & Koyama, M. An Element-Based Generalized Coordination Number for Predicting the Oxygen Binding Energy on Pt3M (M = Co, Ni, or Cu) Alloy Nanoparticles. *ACS Omega* **6**, 3218-3226 (2021).

31. Wang, C. *et al.* Correlation Between Surface Chemistry and Electrocatalytic Properties of Monodisperse Pt_xNi_{1-x} Nanoparticles. *Adv. Funct. Mater.* **21**, 147-152 (2011).

32. Lee, J. D. *et al.* Tuning the Electrocatalytic Oxygen Reduction Reaction Activity of Pt–Co Nanocrystals by Cobalt Concentration with Atomic-Scale Understanding. *ACS Appl. Mater. Interfaces* **11**, 26789-26797 (2019).

Figures and figure legends

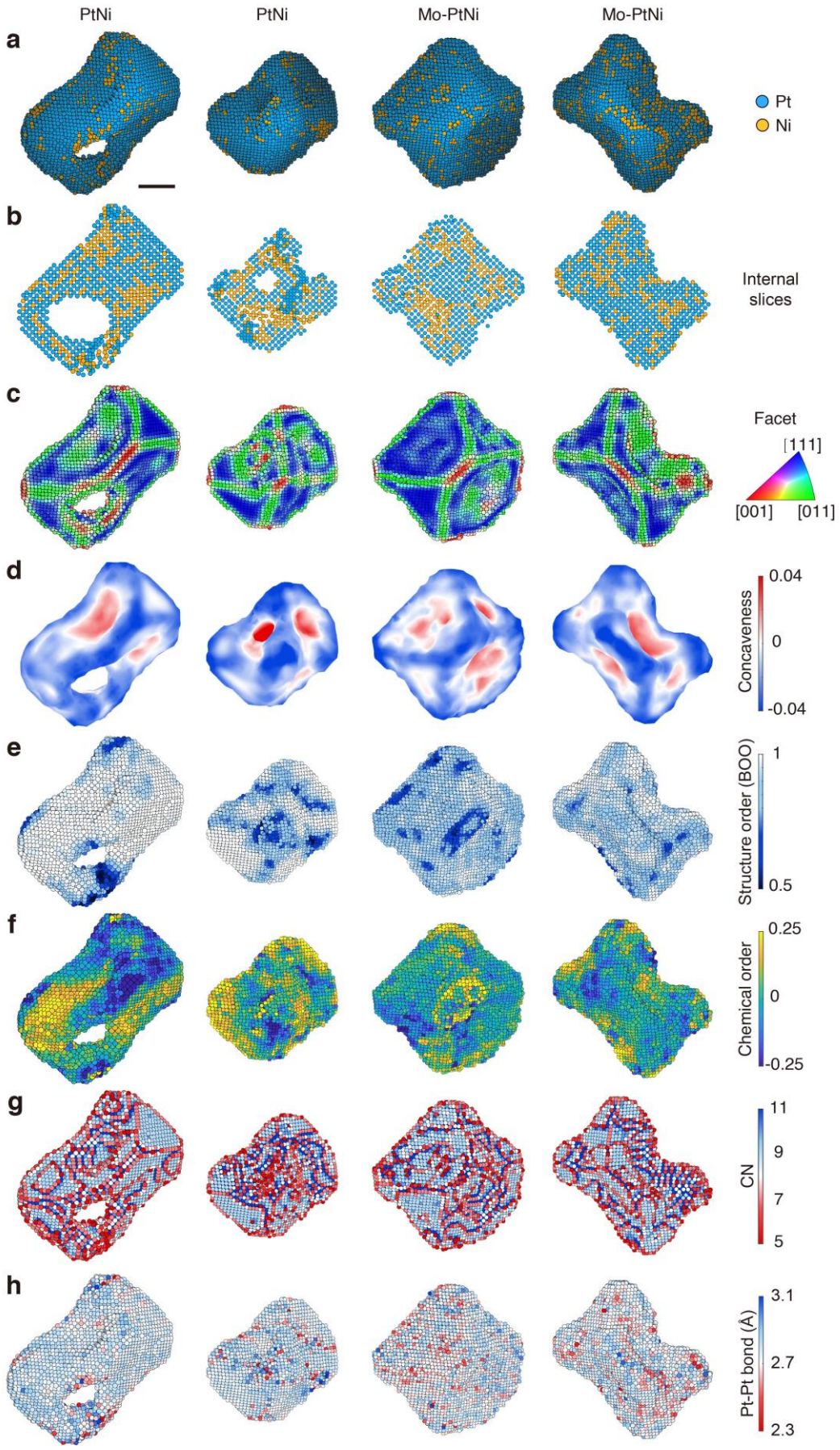
PtNi
PtNi
Mo-PtNi
Mo-PtNi
a
Pt
Ni
b
Internal slices
c
Facet
[111]
[001]
[011]
d
Concaveness
0.04
0
-0.04
e
Structure order (BOO)
1
0.5
f
Chemical order
0.25
0
-0.25
g
CN
11
9
7
5
h
Pt-Pt bond (Å)
3.1
2.7
2.3

256

Figure 1 | 3D atomic structure and chemical composition of four representative nanocatalysts determined by AET. a-h, The 3D surface morphology and chemical composition (**a**), elemental segregation in the interior (**b**), facet (**c**), surface concaveness (**d**), structural order/disorder (**e**), chemical order/disorder (**f**), CN of the surface Pt sites (**g**), and surface bonds (**h**) of the nanocatalysts were quantitatively characterized using the experimental atomic coordinates. For the structural order, BOO = 1 corresponds to a perfect fcc lattice. For the chemical order, positive and negative numbers represent segregation and alloying, respectively. The four nanocatalysts correspond to particles 1-4 from left to right. Scale bar, 2 nm.

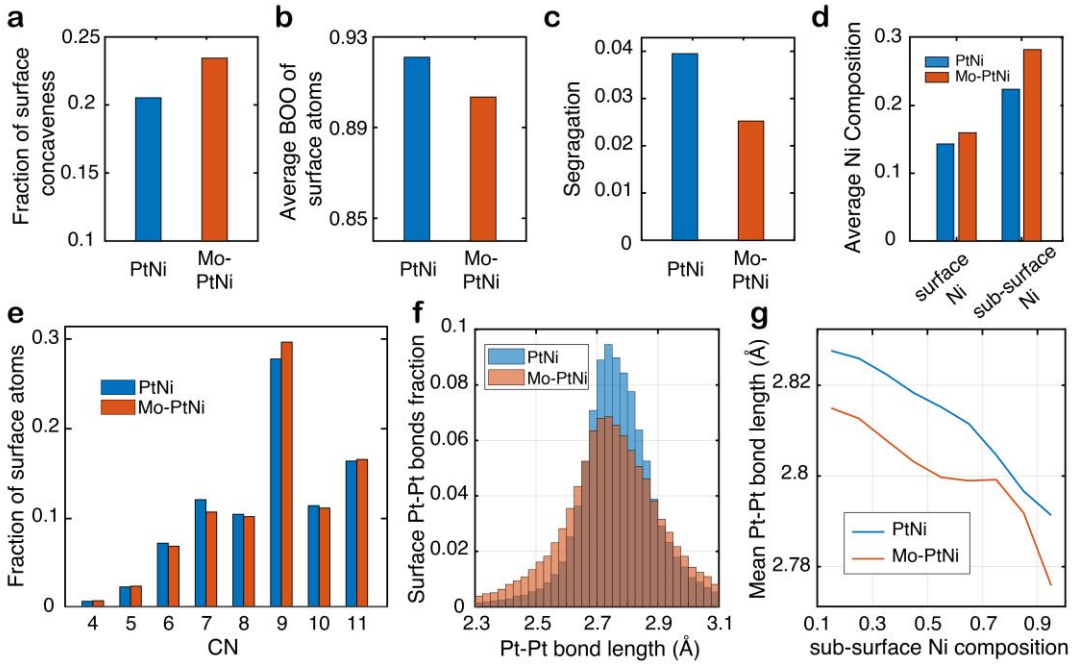

Figure 2 | Quantitative characterization of the PtNi and Mo-PtNi nanocatalysts at the single-atom level. a, Histogram of the fraction of atoms with surface concaveness. **b**, The average BOO distribution of the surface atoms, where BOO = 1 corresponds to a perfect fcc lattice. **c**, The fraction of surface segregation. **d**, Histogram of average surface and subsurface (that is, the layer below the surface) Ni composition. **e**, Distribution of the CN of the surface Pt sites. **f**, Distribution of the surface Pt-Pt bond length. **g**, Correlation between the subsurface Ni composition and the surface Pt-Pt bond length.

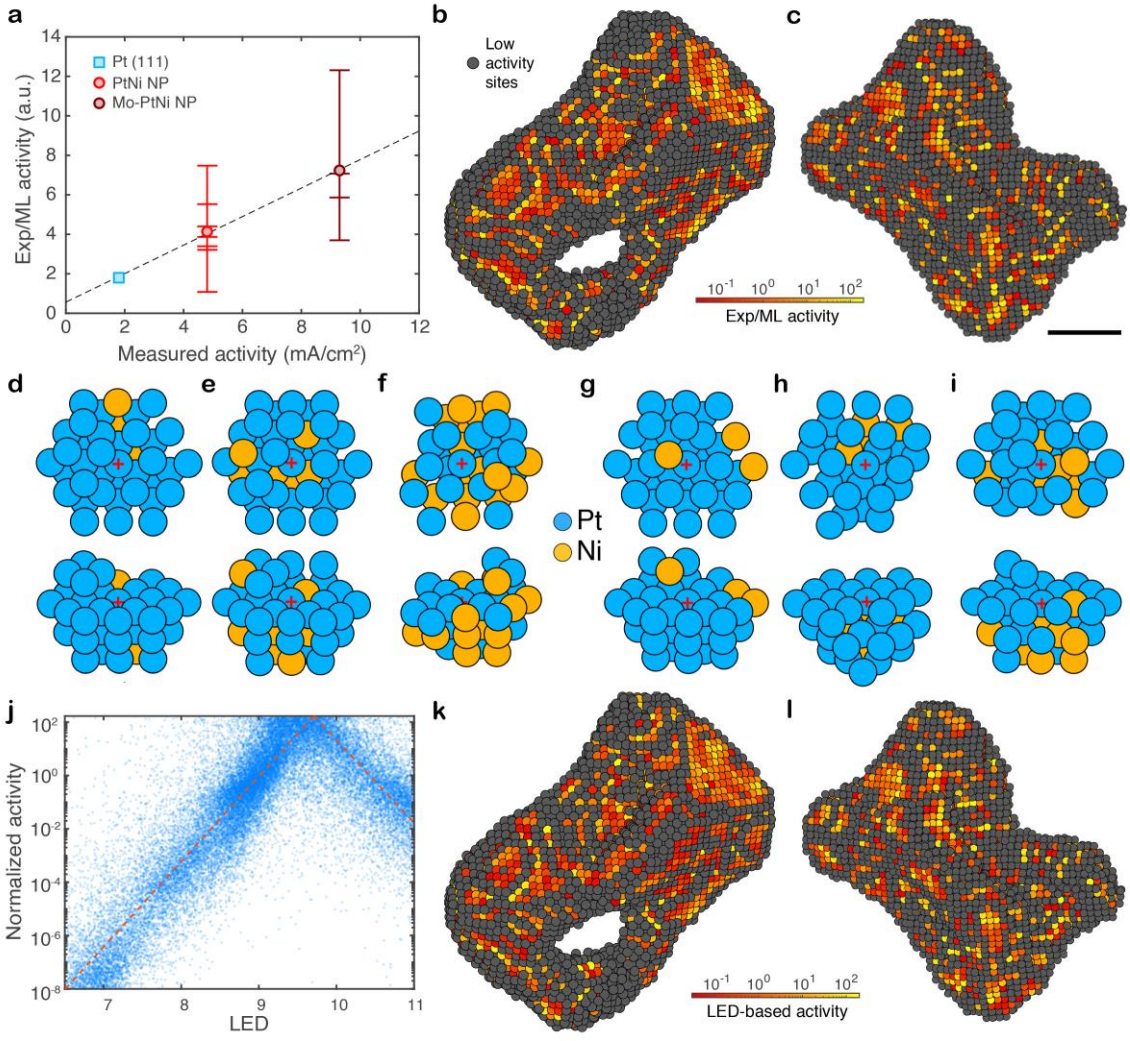

Figure 3 | Identification of the active sites of the nanocatalysts. a, Comparison between the electrochemically measured ORR activity and the ML-identified activity for the experimental 3D atomic coordinates of 11 PtNi and Mo-PtNi nanocatalysts, where each bar represents a nanocatalyst and the circle the average activity. The activity of Pt(111) was obtained from DFT as a reference point. **b**, **c**, The ML-identified activity maps for the experimental 3D atomic coordinates of a PtNi (**b**) and Mo-PtNi (**c**) nanocatalyst, corresponding to particles 1 and 4, respectively, where low activity sites are defined with the ORR activity smaller than 3% of that of Pt(111). Scale bar, 2 nm. **d-i**, Six representative highly active sites (red crosses) on the PtNi (**d-f**) and Mo-PtNi (**g-i**)

nanocatalysts with the ORR activity more than 120 times higher than that of Pt(111). The LED is 9.73, 9.74, 9.7, 9.79, 9.77, 9.75 for (**d-i**), respectively. **j**, Volcano-type activity plot (red dashed line) obtained by fitting the LED with the ML-identified activity of all the surface Pt sites (blue dots), where the peak is at LED = 9.7. **k**, **l**, The LED-based activity maps of the PtNi and Mo-PtNi nanocatalysts (particles 1 and 4, respectively), which are in good agreement with the ML-identified activity maps (**b** and **c**).

METHODS

Chemicals and materials

Platinum(II) acetylacetonate [$Pt(acac)_2$], nickel(II) acetate tetrahydrate [$Ni(ac)_2{\cdot}4H_2O$], benzyl acid (BA) were purchased from Sigma Aldrich. Molybdenum hexacarbonyl ($Mo(CO)_6$), carbon nanotube (CNT) was purchased from Alfa Aesar. N, N-Dimethylformamide (DMF), acetone, isopropanol were purchased from Fisher Scientific. Ethanol was purchased from Decon Labs, Inc. Vulcan XC-72 carbon black (particle size ~50 nm) was from Cabot Corporation. Water used was Ultrapure Millipore (18.2 MΩ·cm).

Sample preparation

Synthesis of Mo-PtNi/C. Vulcan XC-72 carbon black is pre-treated in Argon (80% in volume) and Hydrogen (20% in volume) mixture at 400 C for 4 hours. 80 mg pre-treated Vulcan XC-72 carbon black was dispersed in 60 mL N,N-dimethylformamide (DMF) under ultrasonication for 30 minutes in a 325 mL pressure bottle. Then 64 mg platinum(II) acetylacetonate [$Pt(acac)_2$], 32 mg nickel(II) acetate tetrahydrate [$Ni(ac)_2{\cdot}4H_2O$], and 520 mg benzoic acid were dissolved in 10 mL DMF and were also added into the 325 mL pressure bottle with carbon black dispersion. After ultrasonication for 5 mins, the pressure bottle with well mixed solution was directly put into 140 ºC oil bath and then slowly heated to 160 ºC within 2 hrs. The pressure bottle was kept at 160 ºC for 12 hrs. After 12 hours, 16 mg $Pt(acac)_2$, 8 mg $Ni(ac)_2{\cdot}4H_2O$, 3.2 mg molybdenum(0) hexacarbonyl [$Mo(CO)_6$] were added into the pressure bottle. Then the pressure bottle was kept in 160 ºC oil bath for 48 hrs. After reaction finished, the catalysts were collected by centrifugation, then dispersed and washed with isopropanol and acetone mixture. Then the catalysts were dried in vacuum at room temperature and ready for characterization and electrochemistry test.

Synthesis of PtNi/C. The preparation of procedure is same as Mo-PtNi/C noted above except without adding $Mo(CO)_6$.

Synthesis of Mo-PtNi/CNT. The preparation procedure is same as Mo-PtNi/C noted above except replacing treated Vulcan XC-72 with CNT.

Synthesis of PtNi/CNT. The preparation procedure is same as Mo-PtNi/CNT except without adding $Mo(CO)_6$.

Electrochemical measurements and analysis

A typical catalyst ink was prepared by mixing 2.8 mg of catalyst powder (Mo-PtNi/C, PtNi/C) with 2 mL of ethanol solution containing 16 μL of Nafion (5 wt%) with 5 min ultrasonication time. Then, 10 μL of catalyst ink was dropped onto a 5 mm diameter glassy-carbon electrode (Pine Research Instrumentation). Estimation of Pt loading is based on overall Pt ratio within catalyst determined by ICP-AES. The ink was dried under an infrared lamp; then the electrode was ready for electrochemical test.

A three-electrode cell was used to carry out the electrochemical measurements. The working electrode was a catalyst coated glassy carbon electrode. A Ag/AgCl electrode was used as the reference electrode. A Pt wire with a diameter of 0.05 cm and a length of 23 cm was used as the counter electrode. The geometric exposed surface area of the counter electrode (A_{ce}) is around 3.6 cm^2, which is more than 18 times that of working electrode (A_{we}: 0.196 cm^2). The high A_{ce}/A_{we} ratio was chosen to eliminate the Pt dissolution at counter electrode. The activation procedure was associated with cyclic voltammetry (CV) process, which was conducted in a N_2 saturated 0.1 M $HClO_4$ solution between 0.05 to 1.1 V vs. reversible hydrogen electrode (RHE) at a sweep rate of 100 mV/s for 30 cycles. Oxygen reduction reaction (ORR) measurements were conducted in an O_2 saturated 0.1 M $HClO_4$ solution at a sweep rate of 20 mV/s. iR compensation and background subtraction were applied for ORR test curves following the protocol noted in literature[33]. For the ORR measurement without activation, the prepared working electrode was directly subjected to ORR test in the oxygen saturated electrolyte without being activated at nitrogen saturated electrolyte via CV scan.

The specific activity (SA) is defined as the estimated kinetic current (at 0.9 V vs. RHE) divide by the measured active surface area. The mass activity (MA) is the estimated kinetic current (at 0.9 V vs. RHE) divided by the total Pt mass loaded on the working electrode. The electrochemically active surface area (ECSA) refers to the measured active surface area normalized by the total Pt mass loaded on the working electrode.

Data acquisition

The PtNi and Mo-PtNi nanoparticles were deposited on to 5-nm-thick silicon nitride membranes annealed at 520 °C for 9 minutes in vacuum. A set of tomographic tilt series were acquired from several nanoparticles using the TEAM I microscope. Images were collected at 300 kV in ADF-

STEM mode (Supplementary Table 1). To minimize sample drift, three to five images per angle were measured with 3 μs dwell time. To ensure that no structural changes were observed during the data acquisition, for each nanoparticle, we took the same projection images at zero degree before, during, and after the acquisition of each tilt series. 9 PtNi and 8 Mo-PtNi nanoparticles were measured in this work. The total electron dose of each tilt series for all the nanoparticles were estimated to be between 7.4×10^5 $e^-/Å^2$ and 8.5×10^5 $e^-/Å^2$ (Supplementary Table 1).

Image pre-processing

The image pre-processing consists of the following three steps.

i) *Image registration and drift correction*. We acquired three to five ADF-STEM images at every angle of each tilt series. The images at each angle were registered by cross-correlation. Using first image as a reference, we scanned a cropped region of the subsequent images with a sub-pixel step size and found the drift for every image. After drift correction, we averaged all the images at each angle.

ii) *Image denoising*. The experimental ADF-STEM images have mixed Poisson and Gaussian noise. A generalized denoising algorithm, termed block-matching and 3D filtering (BM3D), was used to denoise each averaged image[34]. The robustness of BM3D on the AET data have been proven in our previous studies[28,35,36].

iii) *Image alignment and background subtraction*. The denoised images of each tilt series were aligned by the centre of mass and common line method as described elsewhere[37]. After alignment, a 2D mask was calculated by the Otsu threshold in MATLAB for each image to match the shape of the nanoparticle. The background was estimated by the discrete Laplacian function in MATLAB. After background subtraction, all the images of each tilt series were re-aligned by the centre of mass and common line to further reduce the error.

3D image reconstruction and refinement

After image pre-processing, each tilt series was reconstructed by an iterative algorithm, termed REal Space Iterative REconstruction (RESIRE)[38]. From the experimental images, RESIRE minimized the L_2-norm error metric using gradient descent. The j^{th} iteration of the algorithm consists of the following steps. RESIRE computed a set of images from the 3D object of the $(j-1)^{th}$ iteration. The difference between the computed and corresponding experimental images was calculated, from which an error metric was defined to monitor the convergence of the algorithm. The difference was back projected to real space, yielding the gradient of the 3D reconstruction. The 3D reconstruction of the j^{th} iteration was updated by combining the gradient with the reconstruction of the $(j-1)^{th}$ iteration, where positivity was enforced as constrains. As a general algorithm, RESIRE is not sensitive to the initial input. After 200 iterations, a preliminary 3D

reconstruction was computed. Based on the preliminary 3D reconstruction, angular refinement and spatial alignment were performed and background subtraction was re-evaluated. After these refinement procedures, a final 3D reconstruction was obtained by running 200 iterations of RESIRE.

Determination of 3D atomic coordinates and chemical species

To increase the precision of atom tracing, we up-sampled each 3D reconstruction by a factor of three using spline interpolation, from which all the local maxima were identified. Starting from the highest intensity, we fit each local maximum of a 9×9×9 voxel volume (1.4×1.4×1.4 $Å^3$) by a 3D polynomial method to locate its centre position[35]. Each fitted local maximum was considered as a potential atom only when its distance from the existing potential atoms is larger than 2 Å. After going through all the local maxima, we obtained a list of potential atoms. For every potential atom, the integrated intensity of the 9×9×9 voxel volume around the centre position was calculated. A K-mean clustering method was used to classify the non-atoms, Pt and Ni atoms[35]. Due to a very small fraction (~0.4%) of Mo atoms in the Mo-PtNi nanoparticles, AET is currently not sensitive enough to distinguish them from Pt or Ni atoms. After excluding the non-atoms and manually checking all the atoms, we obtained an initial 3D atomic model for each 3D reconstruction.

Due to the missing wedge problem[23], we used local re-classification to reduce the effect of the intensity variation in different regions of each 3D reconstruction[35]. At each atomic position, we cropped a 7-Å radius sphere and calculated the mean integrated intensity for the Pt or Ni atom inside the sphere. We then re-classified each atom in the sphere based on the difference between its integrated intensity and the mean value of the Pt or Ni atom. The procedure was repeated until there was no further change.

The electron energy loss spectroscopy maps of the nanoparticles show that there are individual Ni atoms distributed around each nanoparticle (Supplementary Fig. 2). To evaluate the effect of the surrounding Ni atoms on the 3D reconstruction, we simulated a PtNi atomic model in an environment with individual Ni atoms, which used the experimentally determined 3D atomic distribution for the Pt and Ni atom. After calculating projection images at different tilt angles from the model, we performed image pre-processing, conducted the 3D reconstruction, traced the atoms, classified the atomic species and obtained a new 3D atomic model (Supplementary Fig. 8). We observed that there is a layer of ghost atoms surrounding the 3D atomic model, which is due to the surrounding Ni atoms around each nanoparticle (Supplementary Fig. 8d and e). Based on this result, a layer of ghost atoms was removed from the experimental 3D atomic model of each nanoparticle.

X-ray absorption spectroscopy (XAS) data collection and analysis

XAS experiments were conducted on the dry powders of the nanocatalysts studied in this work at the beamline ISS 8-ID in National Synchrotron Light Source II (NSLS) (Brookhaven National Laboratory, NY. Full range Pt L_3-edge and Ni K-edge spectra were collected on the same electrode in transmission mode at the Pt L_3-edge, and/or Ni K-edge, with a Pt or Ni reference foil positioned between I2 and I3 as a reference. Typical experimental procedures were utilized with details provided in our previous work[39]. The data were processed and fitted using the Ifeffit−based Athena[40] and Artemis[41] programs. Scans were calibrated, aligned and normalized with background removed using the IFEFFIT suite[42]. The χ(R) were modelled using single scattering paths calculated by FEFF6[43].

The Pt-Pt bond lengths of nanocatalysts were obtained by the extended x-ray absorption fine structure (EXAFS) fitting. The average first-shell Pt-Pt bond lengths were determined by fitting the EXAFS spectra of dry powders at the Pt L_3 and Ni K-edge simultaneously. S_0^2 was fixed at 0.84 and 0.68 for Pt and Ni, respectively as obtained by fitting the reference foils. Fits were done in *R*-space, $k^{1,2,3}$ weighting. $1.2 < R < 3.1$ Å and $\Delta k = 3.08 - 13.39$ Å^{-1} were used for fitting the Pt L_3-edge data, and $1.3 < R < 3.1$ Å and $\Delta k = 2.56 - 11.40$ Å^{-1} were used for fitting the Ni K-edge data. The fitting results of the E_0 at the Pt L_3 and Ni K edges are 8±2 eV and -6±1 eV, respectively. The EXAFS fit Pt-Pt bond lengths were used to calibrate the voxel size of the AET experiment.

Calculation of the coordination number, facet orientation and surface concaveness

We used custom MATLAB scripts to measure the CN, facet orientation and surface concaveness for all the atomic sites. We defined the nearest-neighbour distance by fitting the valley of the first and second peak of the pair distribution function for each nanocatalyst. The CN was obtained by counting the number of the nearest-neighbour sites within the cutoff distance. Each atom was classified as a surface site if CN < 12 and as an internal site if CN = 12. To find the facet orientation, we derived a density matrix for each nanocatalyst by convolving the atomic structure with a 3D Gaussian function (σ = 4 Å). For each surface site, a normal vector was calculated by computing the gradient of the density matrix at that site. By comparing the normal vectors to the crystallographic directions, we determined the facet orientation of the nanocatalyst. To quantify the surface concaveness, we estimated the surface curvature for all surface sites by using a procedure published elsewhere[44].

The normalized local bond orientational order (BOO) parameter

From the 3D atomic model of each nanoparticle, we calculated the local BOO parameters (Q_4 and Q_6), which are described elsewhere[28,45]. The Q_4 and Q_6 order parameters were computed up to the

second shell with a shell radius of 3.5 Å. We then defined the normalized local BOO parameter as $\sqrt{{Q_4}^2 + {Q_6}^2}/\sqrt{Q_{4\,fcc}^2 + Q_{6\,fcc}^2}$, where $Q_{4\,fcc}$ and $Q_{6\,fcc}$ are the Q_4 and Q_6 values of a perfect fcc lattice. The normalized BOO parameter is between 0 and 1, where 0 means $Q_4 = Q_6 = 0$, and 1 represents a perfect fcc crystal structure.

The chemical order parameter

The chemical order of each nanoparticle was calculated by the pair-wise multicomponent short-range order parameter[46],

$$\alpha_{ij} = \frac{p_{ij} - C_j}{\delta_{ij} - C_j} \qquad (2)$$

where p_{ij} is the probability of finding a *j*-type atom around an *i*-type atom in the first nearest neighbour shell. C_j is the concentration of *j*-type atoms in the nanoparticle and δ_{ij} is the Kronecker delta function. Since there are primarily Pt and Ni atoms in the nanoparticles, all the α_{ij} parameters are correlated. In this study, we chose α_{12} to represent the chemical order parameter. A positive and a negative α_{12} represent segregation and alloying, respectively.

DFT calculations

The DFT calculations were conducted by the VASP package[47-50]. The core electrons were described by the projector-augmented-wave method[51] and the valence states by plane waves up to 400eV. The exchange-correlation interaction of electrons was defined by the Perdew-Bruke-Ernzerhof functional[52]. Spin-polarized calculations were used throughout this manuscript for the PtNi nanocatalysts. The Brillouin zone was sampled by a uniform density of 0.19 $Å^{-1}$ in each reciprocal direction. For isolated clusters, only Γ point was considered. A database of OH adsorption energies on the surface Pt sites of the PtNi model catalysts were computed by DFT (Supplementary Fig. 10). The database includes diverse 3D atomic models consisting of nanoclusters and slabs. The nanoclusters of different sizes were built from truncated octahedra, and the slab models were created from closed-packing surfaces, including fcc(110) surfaces, fcc(100) surfaces and concave shapes similar to these published elsewhere[11]. Ni atoms were introduced by randomly replacing the Pt atoms. The Ni concentration ranges from 0 to 69.6% in the 3D atomic models and from 0 to 83.9% in the local environment (defined as the atoms within the 6.5 Å radius from an adsorption site). Different lattice constants were used to represent tensile and compressive strain. In total, the OH was adsorbed on 207 Pt sites with different Pt CNs, Ni concentration and local environments. The OH binding energy on the Pt sites (BE_{OH}) was computed by,

$$BE_{OH} = E_{OH@Model} - E_{OH} - E_{Model} \qquad (3)$$

where $E_{OH@Model}$ is the total electronic energy of the optimized OH adsorbed structure, E_{OH} is the electronic energy of the OH radical in the gas phase, and E_{Model} is the energy of optimized model without OH adsorption.

Evaluation of the OH binding energy by DFT-trained ML

To evaluate BE_{OH} for all the surface Pt sites, we used a ML method - the Gaussian process regression (GPR)[53]. The ML-GPR method was trained by the DFT-calculated BE_{OH}, and the local atomic environment of the Pt sites was characterized by the smooth overlap of atomic positions (SOAP) approach[54,55]. The cutoff radius of 6.5 Å was selected in SOAP, which was later validated by the accurate prediction of the ML-GPR method (Supplementary Fig. 11). The GPR was implemented by the Python-scikit package[56]. The kernel function is defined as normalized polynomial kernel of the partial power spectrum,

$$K(\mathbf{d}_1, \mathbf{d}_2) = \left(\frac{\mathbf{d}_1^{\mathrm{T}} \mathbf{d}_2}{\sqrt{\mathbf{d}_1^{\mathrm{T}} \mathbf{d}_1 \mathbf{d}_2^{\mathrm{T}} \mathbf{d}_2}} \right)^{\zeta} \qquad (4)$$

Where $K(\mathbf{d}_1, \mathbf{d}_2)$ is the kernel function between SOAP descriptors $\mathbf{d_1}$ and $\mathbf{d_2}$, and ζ is a hyperparameter. In this study, we chose $\zeta = 4$ by balancing the accuracy and transferability. We trained the GPR by randomly choosing 134 atomic models and then used the ML method to predict the BE_{OH} of the remaining 73 atomic models. The RMSE is 0.05 and 0.07 eV per site for the training and test set, respectively (Supplementary Fig. 11). The small REMS values indicate the robustness of the ML method. After validating DFT-trained ML, we applied it to evaluate the BE_{OH} of the surface Pt sites of the 7 PtNi and 4 Mo-Pt/Ni nanocatalysts.

Estimation of the ORR activity based on the OH binding energy

From the ML-identified BE_{OH}, we estimated the ORR activity of each surface Pt site by calculating ΔBE_{OH},

$$\Delta BE_{OH} = BE_{OH} - BE_{OH,Pt(111)} \qquad (5)$$

where $BE_{OH,Pt(111)}$ is the OH binding energy of Pt(111). As the ORR activity and ΔBE_{OH} are related to each other by the volcano-type plot[29,57,58], we evaluated the current density of the ORR oxygen using formulas published elsewhere[57]. On the left side of the volcano plot, we computed the current density of the ORR for the i^{th} surface Pt site (j_i) by,

$$kT \ln\left(\frac{j_i}{j_{Pt(111)}}\right) = \Delta BE_{OH,i} \qquad (6)$$

where k is the Boltzmann constant, T the temperature, $j_{Pt(111)}$ the current density of the ORR for Pt(111), and $\Delta BE_{OH,i}$ the OH binding energy difference (Eq. (5)) for the i^{th} surface Pt site. We computed the current density of the ORR on the right side of the volcano plot by,

$$kT\ln\left(\frac{j_k}{j_{Pt(111)}}\right) = 0.26 - 0.97 \cdot \Delta BE_{OH,k} \qquad (7)$$

where k represents the k^{th} surface Pt site. Based on Eqs. (6) and (7), the current density of any surface Pt site is obtained by,

$$j = \min(j_i, j_k)\ . \qquad (8)$$

Figure 3b, c, Supplementary Fig. 12 and Video 2 shows the ML-identified activity of all the surface Pt sites (blue dots) for the 7 PtNi and 4 Mo-Pt/Ni nanocatalysts. We observed that the ORR activity of the various surface Pt atoms differs by several orders of magnitude. The average activity of these nanocatalysts is in good agreement with the electrochemically measured activity (Fig. 3k, l, Supplementary Fig. 13 and Video 2).

Derivation of the LED equation

We derived the LED by fitting a large number of experimentally measured structural and chemical properties to the ΔBE_{OH} of the surface Pt sites of the 7 PtNi and 4 Mo-Pt/Ni nanocatalysts. The fitting variables include the CN, the surface CN, the sub-surface CN, the average Pt-Pt bond length around each Pt site ($\bar{d}_{Pt}$), the structure/chemical order parameter, the nearest-neighbor Pt and Ni atoms of each surface Pt atom (NN^{Pt} and NN^{Ni}), the generalized CN ($\overline{CN}$), the element-based $\overline{CN}$ ($\overline{CN}^{Pt}$ and $\overline{CN}^{Ni}$), etc. We examined the 2, 3 and 4 variable LED equations to minimize the RMSE by,

$$RMSE = \sqrt{\frac{\sum_{i=1}^{N}\left(\Delta BE_{OH,i}^{ML} - \Delta BE_{OH,i}^{Cal}\right)^2}{N}} \qquad (9)$$

where $\Delta BE_{OH,i}^{ML}$ is the ΔBE_{OH} of the i^{th} surface Pt site obtained by ML, N is the total number of the surface Pt sites, and $\Delta BE_{OH,i}^{Cal} = E_1 * LED - E_0$ with E_1 and E_0 are two fitting constants. For the 2 variable LED equation, we examined $LED = a_1x_1 + a_2x_2$, where a_1 and a_2 are two fitting constants, x_1 and x_2 are two fitting variables. We obtained the smallest RMSE value of 0.117 eV by choosing $x_1 = CN$ and $x_2 = e^{-\bar{d}_{Pt}}$. For the 3-variable LED equation, we found that $LED = a_1x_1 * x_2 + a_2x_3$ produces the smallest RMSE value of 0.104 eV with $x_1 = NN^{Pt}$, $x_2 = e^{-\bar{d}_{Pt}}$ and $x_3 = \overline{CN}^{Ni}$ (Supplementary Table 2). For the 4-variable LED equation, we examined $LED = a_1x_1 * x_2 + a_2x_3 * x_4$ and $LED = a_1x_1 * x_2 + a_2x_3 + a_3x_4$. After testing all the fitting variables, we derived an optimized equation, $LED = a_1x_1 * x_2 + a_2x_3$, with the RMSE of 0.104 eV. We revised the equation to be $LED = NN^{Pt} \cdot e^{-a_1 \cdot \varepsilon} + a_2 \cdot \overline{CN}^{Ni}$, where $\varepsilon = \frac{\bar{d}_{Pt} - d_0}{d_0}$ and $d_0 =$ 2.75 Å is the Pt-Pt bond length of the Pt nanoparticles. The revision only changed the fitting constants, but not the RMSE. With this LED equation, we have $a_1 = 1.985$, $a_2 = 1.075$, $E_1 = 0.189$, $E_0 = 0.1703$, and RMSE = 0.104 eV.

Data availability

All the raw and processed experimental data will be posted on https://github.com, which can be freely downloaded, immediately after the paper is published. The 3D atomic coordinates of PtNi and Mo-PtNi nanoparticles will be deposited in the Materials Data Bank (www.materialsdatabank.org) immediately after the paper is published.

Code availability

All the MATLAB source codes for the 3D image reconstruction, atom tracing, refinement and data analysis of this work will be posted on https://github.com, immediately after the paper is published.

33. Shinozaki, K., Zack, J. W., Richards, R. M., Pivovar, B. S. & Kocha, S. S. Oxygen Reduction Reaction Measurements on Platinum Electrocatalysts Utilizing Rotating Disk Electrode Technique. *J. Electrochem. Soc.* **162**, F1144-F1158 (2015).
34. Dabov, K., Foi, A., Katkovnik, V. & Egiazarian, K. Image Denoising by Sparse 3-D Transform-Domain Collaborative Filtering. *IEEE Transactions on Image Processing* **16**, 2080-2095 (2007).
35. Yang, Y. *et al.* Deciphering chemical order/disorder and material properties at the single-atom level. *Nature* **542**, 75-79 (2017).
36. Zhou, J. *et al.* Observing crystal nucleation in four dimensions using atomic electron tomography. *Nature* **570**, 500-503 (2019).
37. Chen, C.-C. *et al*. Three-dimensional imaging of dislocations in a nanoparticle at atomic resolution. *Nature* **496**, 74-77 (2013).
38. Pham, M., Yuan, Y., Rana, A., Miao, J. & Osher, S. RESIRE: real space iterative reconstruction engine for Tomography. *arXiv:2004.10445* (2020).
39. Jia, Q. *et al.* Activity Descriptor Identification for Oxygen Reduction on Platinum-Based Bimetallic Nanoparticles: In Situ Observation of the Linear Composition–Strain–Activity Relationship. *ACS Nano* **9**, 387-400 (2015).
40. Newville, M. IFEFFIT : interactive XAFS analysis and FEFF fitting. *Journal of Synchrotron Radiation* **8**, 322-324 (2001).
41. Ravel, B. & Gallagher, K. Atomic Structure and the Magnetic Properties of ZrDoped Sm2Co17. *Phys. Scr.*, 606 (2005).
42. Newville, M., Līviņš, P., Yacoby, Y., Rehr, J. J. & Stern, E. A. Near-edge x-ray-absorption fine structure of Pb: A comparison of theory and experiment. *Phys. Rev. B* **47**, 14126-14131 (1993).

43. Ankudinov, A. L., Ravel, B., Rehr, J. J. & Conradson, S. D. Real-space multiple-scattering calculation and interpretation of x-ray-absorption near-edge structure. *Phys. Rev. B* **58**, 7565-7576 (1998).
44. Do Carmo, M. P. *Differential geometry of curves and surfaces (2nd ed.)* (Courier Dover Publications, 2016).
45. Lechner, W. & Dellago, C. Accurate determination of crystal structures based on averaged local bond order parameters. *J. Chem. Phys.* **129**, 114707 (2008).
46. Li, Q.-J., Sheng, H. & Ma, E. Strengthening in multi-principal element alloys with local-chemical-order roughened dislocation pathways. *Nat. Commun.* **10**, 3563(2019).
47. Kresse, G. & Hafner, J. Ab initio molecular dynamics for liquid metals. *Phys. Rev. B* **47**, 558-561 (1993).
48. Kresse, G. & Hafner, J. Ab initio molecular-dynamics simulation of the liquid-metal--amorphous-semiconductor transition in germanium. *Phys. Rev. B* **49**, 14251-14269 (1994).
49. Kresse, G. & Furthmüller, J. Efficient iterative schemes for ab initio total-energy calculations using a plane-wave basis set. *Phys. Rev. B* **54**, 11169-11186 (1996).
50. Kresse, G. & Furthmüller, J. Efficiency of ab-initio total energy calculations for metals and semiconductors using a plane-wave basis set. *Computational Materials Science* **6**, 15-50 (1996).
51. Kresse, G. & Joubert, D. From ultrasoft pseudopotentials to the projector augmented-wave method. *Phys. Rev. B* **59**, 1758-1775 (1999).
52. Perdew, J. P., Burke, K. & Ernzerhof, M. Generalized Gradient Approximation Made Simple. *Phys. Rev. Lett.* **77**, 3865-3868 (1996).
53. Rasmussen, C. E. in *Summer School on Machine Learning*. pp. 63-71 (Springer, 2003).
54. Himanen, L. *et al.* DScribe: Library of descriptors for machine learning in materials science. *Comput. Phys. Commun.* **247**, 106949 (2020).
55. Bartók, A. P., Kondor, R. & Csányi, G. On representing chemical environments. *Phys. Rev. B* **87** (2013).
56. Pedregosa, F. *et al*. Scikit-learn: Machine learning in Python. *J. Mach. Learn. Res*. **12**, 2825-2830 (2011).
57. Viswanathan, V., Hansen, H. A., Rossmeisl, J. & Nørskov, J. K. Universality in Oxygen Reduction Electrocatalysis on Metal Surfaces. *ACS Catal.* **2**, 1654-1660 (2012)
58. Hansen, H. A., Viswanathan, V. & Nørskov, J. K. Unifying Kinetic and Thermodynamic Analysis of 2 e^- and 4 e^- Reduction of Oxygen on Metal Surfaces. *J. Phys. Chem. C* **118**, 6706-6718 (2014)

Acknowledgments This work was primarily supported by the US Department of Energy (DOE), Office of Science, Basic Energy Sciences (BES), Division of Materials Sciences and Engineering under award DE-SC0010378 (including AET experiments, 3D image reconstruction, atom tracing, classification and data analysis). It was also partially supported by STROBE: A National Science Foundation Science & Technology Center under grant number DMR 1548924 and the NSF DMREF under award number DMR-1437263. G.S. and P.S. acknowledge the support by DOE-BES grant DE-SC0019152. AET experiments were performed with TEAM I at the Molecular Foundry, which is supported by the Office of Science, Office of Basic Energy Sciences of the US DOE under contract number DE-AC02-05CH11231. The XAS experiment was conducted on beamline 8-ID (ISS) of the National Synchrotron Light Source II, which is supported by the Office of Science, Office of Basic Energy Sciences of the US DOE under contract number DE-SC0012704.

Author contributions J.M. directed the project; Z.Z., Y.L. and Y.H. synthesized the samples and performed the ORR test; J.Z., P.E., J.C. and J.M. discussed and/or conducted the AET experiments; Q.J. and Q.S. did the XAS experiment; Yao Yang, Yongsoo Yang, Y. Yuan and J.M. performed 3D image reconstruction, atom tracing and classification; G.S., Z.Y., and P.S. carried out the DFT calculations and implemented the ML method with input from Yao Yang, C.O. and J.M.; Yao Yang, J.Z., Z.Z., G.S., C.O., S.M., C.Z., H.H., P.S., Y.H. and J.M. analyzed and/or interpreted the results J.M., Yao Yang, S.M. Z.Z. and G.S. wrote the manuscript. All authors commented on the manuscript.

Competing interests The authors declare no competing interests.

Supplementary Files

This is a list of supplementary files associated with this preprint. Click to download.

- Miaosupplementaryinfo.docx
- Video1.mov
- Video2.mov